Title: Miniature Magneto-Mechanical Resonators for Wireless Tracking and Sensing

Authors: Bernhard Gleich[1], Ingo Schmale[1], Tim Nielsen[1], and Jürgen Rahmer[1]*

Affiliations:

[1]Philips Research; Hamburg, Germany

*Corresponding author. Email: juergen.rahmer@philips.com

Abstract:

Sensor miniaturization enables applications like minimally invasive medical procedures or patient monitoring by providing feedback of the process in-situ. Ideal miniature sensors should be wireless, inexpensive, and allow for remote detection over sufficient distance by an affordable detection system. We analyze the signal strength of wireless sensors theoretically and derive a simple design of high-signal resonant magneto-mechanical sensors featuring volumes below 1 mm³. As examples, we demonstrate real-time tracking of position and attitude of a flying bee, navigation of a biopsy needle, tracking of a free-flowing marker, and sensing of pressure and temperature, all in unshielded environments. The achieved sensor size, measurement accuracy, and workspace of about 25 cm show the potential as a low-cost wireless tracking and sensing platform for medical and non-medical applications.

One-Sentence Summary: Low frequency resonant magneto-mechanical sensors smaller than 1 mm³ can be reliably detected up to 25 cm.

Main Text:

The rise of minimally invasive procedures has created a need for tracking medical instruments inside the human body, which is currently satisfied by cabled electro-magnetic (EM) trackers (*1*), optical tracking approaches based on cameras (*2*) or optical fibers (*3*), imaging-based markers (*4*), and wireless radiofrequency (RF) markers (*5*). Specific drawbacks of each of the methods, however, limit their general usability. Not all body locations can be reached with a wire, an optical line of sight is usually not available inside the human body, imaging equipment is costly or may use harmful radiation, and wireless RF markers require a minimal size of roughly 10 mm to accommodate an antenna for communication with a detector outside the body (*5*). Another field that suffers from current technology limitations is the data-driven evaluation of physiological parameters (*6*), e.g., for early detection of disease but also for monitoring patients at home to reduce time in hospital (*7*). In these applications, small low-cost sensors are required to continuously monitor and report physiological parameters not only from the surface (*8*) but also from inside of the human body. Based on theoretical insights, we designed a technology platform that can address these needs by combining existing technologies with miniaturized sensors of about 1 mm in size. The platform may serve many applications, e.g., the navigation of surgical devices and catheters (*2*), home monitoring of blood pressure (*9*), radiation-free gastric emptying studies (*10*), controlling oral medication adherence (*11*, *12*), monitoring insect behavior (*13*, *14*), or labelling of goods with MMRs acting as micro RFID tags (*15*).

The basic concept of the magneto-mechanical resonator (MMR) is displayed in Fig. 1A. The resonator consists of two spherical NdFeB magnets (*16*), one of them fixed to the cylindrical housing, the other one suspended from a thin filament. It is held in place by the magnets' mutual attractive force, which surpasses the gravitational force by 3 orders of magnitude. The torque exerted by the fixed magnet's field drives the magnetic moments into an anti-parallel alignment. To start a rotational oscillation, an external magnetic field pulse is applied, whose torque creates an angular deflection of the suspended sphere (Movie S1 / white double arrow in Fig. 1A). The oscillation frequency is determined by the restoring torque provided by the fixed sphere and thus depends on the distance between the spheres. The principle of our MMR detection system is described in Fig. 1B. It generates current pulses that are transmitted via electromagnetic coils (Fig. 1C) to excite the MMR oscillation. The oscillating magnetic moment then induces a voltage in these coils which, after amplification, represents the received signal. The low friction in the MMR filament bearing translates into a slow signal decay, so that short excitation periods can alternate with long windows for signal acquisition. Fig. 1D displays the voltage induced in one of the 16 receive coils by an MMR resonating at 2.2 kHz. It is repeatedly excited by short pulse trains. Before each re-excitation, the system performs a real-time evaluation of the acquired data to adjust excitation pulse frequency, phase, and amplitude for optimal build-up of the MMR oscillation. The signals obtained from the different coils uniquely encode spatial position and orientation of the MMR. Since the planar oscillation of the magnetization vector creates two orthogonal signal components (cf. supplementary materials), the position and full orientation information, i.e., 6 degrees of freedom (DoF), can be reconstructed using the known spatial sensitivity profiles of the coils.

While the signal amplitude distribution over the coils is used for tracking, the frequency of the MMR signal does not carry spatial information. It can be used to measure a physical parameter that changes distance between the two magnetic spheres and thus modulates the oscillation frequency. Examples are temperature via thermal expansion or pressure via a compressible housing. Materials that respond to radiation or certain chemicals enable dosimeters or chemical sensors, respectively.

Results

To highlight the small marker footprint, a bee equipped with an MMR (weight about 1.5 mg) is tracked in real-time while walking and flying at distances up to 200 mm from the coil array (Fig. 2 and movies S2 / S3). The raw measurement rate is about 40 Hz and each measurement delivers the bee's momentary position (*x*, *y*, *z*) and attitude (pitch, yaw, roll), i.e., 6-DoF information. According to both the tracking data and camera view, the flying bee achieved velocities up to 600 mm/s.

For demonstrating medical navigation, an MMR is integrated in a stylet that is inserted in a curved biopsy needle (Fig. 3A). Due to the low resonance frequency of 2.2 kHz, the titanium alloy of the needle only weakly attenuates the MMR signal. Therefore, accurate needle tip tracking over the volume of a gelatin phantom (Fig. 3B, diameter 135 mm) is possible, with a distance of about 140 mm between needle and coil array. The 6-DoF information enables accurate navigation of the needle towards a target (Fig. 3C and Movie S4). Navigation could be fully based on a "roadmap" provided by a medical imaging system whose frame of reference is aligned with the tracking system. No line of sight to the needle tip is required and the camera view has only been included for reference. To simulate tracking of an ingestible marker during gastro-intestinal passage, an untethered MMR is localized while flowing through a winding tube phantom (supplementary Fig. S5 and Movie S7).

To demonstrate sensing, a sealed MMR pressure sensor is subjected to pressure changes (Fig. 4). The diffusion-tight metallic housing (Fig. 4A) is compressible like a common aneroid barometer. Sensitivity and measurement range of the sensor can be tuned via the stiffness of the housing. The sensor uses two oscillating spheres to reduce sensitivity to static magnetic background fields. Fig. 4B shows the resonance frequency extracted from the measured signal while pressure changes are applied manually using a syringe. For reference, the pressure measured by a commercial pressure sensor is plotted in Fig. 4C, showing that frequency directly represents pressure. A pressure range of 400 mbar (300 mmHg) is covered, which is sufficient for a blood pressure sensor (*9*) and leaves room for pressure offsets due to different geographic altitudes. Sensitivity of the sensor is 0.34 Hz/mbar. Fig. S4 and Movie S5 show that the tracking marker of the needle navigation experiment can also be used for measuring temperature.

Scaling Laws

The experiments demonstrate MMR tracking and sensing using millimeter-sized devices. This miniaturization was achieved by designing the MMRs for maximal signal. For comparison with existing technology, we compare the signal of MMRs with conventional passive RF circuits. RF circuits are also called LC resonators, since the resonant circuit contains an inductor L and a capacitor C, with the inductor acting as an antenna (circuit diagram in Fig. S3A) (*5*, *9*). For generating a signal that is detectable during the acquisition phase, MMRs and LC resonators must first be driven to sufficiently high oscillation amplitudes using excitation fields of amplitude B_1 at the device resonance frequency f_0. The dominant limiting factor to the applicable field amplitude is the rate of field change $R = 2\pi f_0 B_1$ that describes the magnitude of field change per time. R determines how much voltage is induced in surrounding materials and is thus restricted by safety limits on touch voltages on metallic surfaces and by physiological limits like peripheral nerve stimulation (PNS) and tissue heating (specific absorption rate, SAR) (*17*, *18*). To quantify the achievable signal, we introduce a normalized device signal Σ as a function of rate R and radius r of the field generating element in the wireless device.

For MMRs, r is the radius of the oscillating spherical magnet (cf. Fig. 5A) and the key finding is the proportionality:

$$\Sigma_{\mathrm{MMR}} \propto R^{\frac{1}{3}} r^{\frac{7}{3}} \quad . \tag{1}$$

For LC resonators, r is the outer radius of the coil element (cf. Fig. 5B) and the device signal scales as:

$$\Sigma_{\mathrm{LC}} \propto R\, r^{5} \quad . \tag{2}$$

The complete formulae and their derivation are found in the supplementary materials.
Fig. 5C displays device signals Σ_{MMR} and Σ_{LC} as a function of r for different rates of field change R. In view of safety regulations, a rate of $R \approx 1000$ mT/s at the device position is assumed to be the highest tolerable rate in the frequency range between a few kHz and 100 MHz. The combination of this limit with a minimal detectable signal threshold leads to triangular regions in the plots, indicating the signal / size combinations which the technology can provide. For LC resonators, the triangular operating region is shaded in blue, whereas the region for MMR devices is shaded in green. According to the scaling laws, the operating region for the MMRs extends to smaller device sizes. The needle tracking experiment is indicated as "MMR". Due to power limitations of the transmit amplifiers of our detection system, it does not fully exploit the theoretical size reduction potential for this signal level. For comparison, an LC resonator would need to be almost an order of magnitude larger in linear dimension *r* to reach the same signal level.
For sensing applications, information is encoded in frequency and therefore frequency resolution Δf relates to measurement accuracy. For assessing sensor performance, the device signal Σ must thus be weighted with a quality function ζ coupled to frequency resolution, as described in the methods section. The respective products $\Sigma \cdot \zeta$ are plotted in Fig. 5D, showing that the relative miniaturization potential of MMR technology compared to LC technology is even higher for sensors than for markers.

Discussion and Conclusion

The MMR technology enables miniaturization of wireless markers and sensors by about an order of magnitude in linear dimension compared to existing LC resonator technology, while the required field generator and detection system have a similar footprint. The marker used in the needle tracking experiment has a length of 1.9 mm, whereas an LC-based product with similar workspace has a length of 8 mm (*5*). Commercial miniature RFID tags used in bee experiments (*13*) have a similar size as the MMR but provide so little signal that they can be detected only up to a few millimeters. The MMR pressure sensor has a length of 1.8 mm compared to a length of 11 mm for the coil element of a commercial miniature pressure sensor (*9*).
Miniaturization is enabled by the high MMR signal, which results from several aspects (cf. Eq. S1 in materials and methods): First, the high magnetization of NdFeB permanent magnets (*16*) leads to an efficient energy transfer to and from the MMR. Second, the low dissipation in the filament minimizes energy losses and results in very high quality factors. Third, the filament bearing allows high angular oscillation amplitudes of the suspended sphere, leading to large magnetization changes that induce high voltages in the detection coils. Fourth, the magnetic restoring torque provided by the second magnet corresponds to a low stiffness or torsion constant that results in a rather low resonance frequency when compared to purely mechanical resonators. When the rate of excitation field change is limited, which is the case in most practical applications, a lower frequency enables higher angular oscillation amplitudes and thus increased signal. Our mathematical derivation shows that frequencies around a few kilohertz are optimal for MMRs, whereas much higher frequencies are optimal for LC resonators. Low frequencies

have the benefit of inducing fewer eddy currents in metallic objects or a patient body and thus reduce shielding effects. This is demonstrated in the curved needle experiment, where the MMR is detected inside a metallic needle.

The MMR design also overcomes limitations encountered by magnetic micro-electro-mechanical systems (MEMS) for wireless actuation and sensing applications (*19*–*21*). MEMS processes are limited to low remanence magnetic materials and resonators typically use rather stiff mechanical elements, resulting in high frequencies but low oscillation amplitudes, leading to low signal. Furthermore, dissipation in mechanical elements is generally higher than in magnetic restoring elements, which limits MEMS quality factors and thus frequency resolution for sensing applications.

The simplicity of MMRs may enable simple manufacturing and low cost. The housing can be made from glass or plastic; the filament and the NdFeB magnets are also inexpensive. The MMR assembly does not require high precision, as the magnetic forces automatically center the oscillating sphere. These benefits combined with the small size of MMRs and their wireless detection distance of about 25 cm (cf. supplemental materials Fig S6) could improve or enable a wide range of applications.

One potential medical application could be medication adherence control, where an MMR is integrated in a pill whose presence can be detected wirelessly inside a patient's gastro-intestinal (GI) tract. Existing approaches either require detection patches with body contact (*11*) or centimeter-sized electronic pills (*12*). MMR tracking in the GI tract as simulated by the phantom experiment in the supplementary materials (Fig. S5, Movie S7) could furthermore deliver dynamic information on gastric emptying (*10*) and bowel motility (*22*). Here, several MMR markers with different resonance frequencies could be operated in parallel to collect information from many locations simultaneously; an advantage over magnetic tracking technologies using larger static magnets *(23, 24)*. A proof-of-principle experiment on simultaneous tracking of 3 MMRs operating at different frequencies is presented in Fig. S7 and Movie S8. Furthermore, MMR sensing in the GI tract could simultaneously deliver body core temperature (*25*), peristaltic pressure, pH value, or bowel content viscosity. In surgical applications, MMRs could be used for marking tumor tissue to guide excision. Current non-radioactive solutions require larger markers while having a smaller detection distance than MMRs (*26*, *27*). For monitoring and telemedicine solutions, tiny MMR sensors could be operated directly in the blood stream, e.g., for measuring physiological parameters like blood pressure (*9*) or for functional monitoring of implanted devices, e.g., early detection of clogging in vascular stents.

MMRs could also be added to medical instruments such as needles, catheters, guidewires, or bronchoscopes to simplify in-body navigation (*2*) without the need for imaging, which is costly and often involves harmful X-ray radiation. The magnetic detection mechanism avoids line-of-sight problems of camera-based tracking systems. In addition, wireless MMRs promise simpler integration in devices and better workflow than cable- or fiber-dependent solutions (*3*). Furthermore, position and full orientation information (6 DoF) can be retrieved from a single MMR. With wireless LC resonators (*5*) or conventional wired electromagnetic tracking coils (*28*), at least two markers must be combined to deliver all three angles that determine orientation in space.

MMR technology could also be useful in non-medical applications, e.g., RFID tagging. Millimeter-sized MMRs could be integrated in products and consumables where current RFID tags are either too large or too limited in detection distance. For identification, differences in resonance frequency, damping constant, magnetic dipole moment, and various non-linear properties could be used to discern millions of MMRs by their signal response.

There are limitations of the MMR technology that may impact certain applications. A general limitation is the achievable signal level versus noise and background signals. While our demonstrations were performed with millimeter-sized MMRs up to a distance of about 25 cm in an unshielded environment, a potential need for even smaller devices, higher accuracy, or larger workspaces may require advanced background signal subtraction strategies. The system could also be operated in a shielded environment, which would allow miniaturization of the magnetic elements to a few micrometers (*29*). Further limitations are systematic errors caused by nearby ferromagnetic or metallic objects. Stray fields from ferromagnets can shift the MMR resonance frequency and affect sensing accuracy. Eddy currents induced in metals can distort the dynamic magnetic fields and thus affect localization accuracy, an effect shared with wire-bound electromagnetic tracking (*2*). A limitation for tracking of very fast objects, such as a flying bee, are position and orientation changes occurring within the signal acquisition window.

In conclusion, the presented MMR design enables shrinking wireless markers and sensors to the millimeter range while maintaining sufficient signal and sensitivity for remote detection. Demonstrations of tracking, device navigation, and sensing show the potential for a platform technology that can cover a wide range of applications.

References

1. A. M. Franz *et al.*, Electromagnetic Tracking in Medicine—A Review of Technology, Validation, and Applications. *IEEE Transactions on Medical Imaging*. **33**, 1702–1725 (2014).
2. A. Sorriento *et al.*, Optical and Electromagnetic Tracking Systems for Biomedical Applications: A Critical Review on Potentialities and Limitations. *IEEE Reviews in Biomedical Engineering*. **13**, 212–232 (2020).
3. C. Shi *et al.*, Shape Sensing Techniques for Continuum Robots in Minimally Invasive Surgery: A Survey. *IEEE Transactions on Biomedical Engineering*. **64**, 1665–1678 (2017).
4. D. Kessel, I. Robertson, T. Sabharwal, *Interventional radiology: a survival guide* (Churchill Livingstone, Elsevier, Edinburgh London New York Oxford, 3. edition., 2011).
5. T. R. Willoughby *et al.*, Target localization and real-time tracking using the Calypso 4D localization system in patients with localized prostate cancer. *International Journal of Radiation Oncology*Biology*Physics*. **65**, 528–534 (2006).
6. C. Orphanidou, A review of big data applications of physiological signal data. *Biophys Rev*. **11**, 83–87 (2019).
7. S. P. Radhoe, J. F. Veenis, J. J. Brugts, Invasive Devices and Sensors for Remote Care of Heart Failure Patients. *Sensors*. **21**, 2014 (2021).
8. M. Lin, H. Hu, S. Zhou, S. Xu, Soft wearable devices for deep-tissue sensing. *Nat Rev Mater*, 1–20 (2022).
9. W. T. Abraham *et al.*, Safety and accuracy of a wireless pulmonary artery pressure monitoring system in patients with heart failure. *American Heart Journal*. **161**, 558–566 (2011).
10. J. Keller *et al.*, Advances in the diagnosis and classification of gastric and intestinal motility disorders. *Nat Rev Gastroenterol Hepatol*. **15**, 291–308 (2018).
11. H. Hafezi *et al.*, An Ingestible Sensor for Measuring Medication Adherence. *IEEE Trans. Biomed. Eng.* **62**, 99–109 (2015).
12. P. R. Chai *et al.*, Digital Pills to Measure Opioid Ingestion Patterns in Emergency Department Patients With Acute Fracture Pain: A Pilot Study. *Journal of Medical Internet Research*. **19**, e7050 (2017).
13. S. Streit, F. Bock, C. W. W. Pirk, J. Tautz, Automatic life-long monitoring of individual insect behaviour now possible. *Zoology*. **106**, 169–171 (2003).
14. J. D. Crall *et al.*, Neonicotinoid exposure disrupts bumblebee nest behavior, social networks, and thermoregulation. *Science*. **362**, 683–686 (2018).
15. V. Chawla, D. S. Ha, An overview of passive RFID. *IEEE Communications Magazine*. **45**, 11–17 (2007).
16. J. J. Croat, J. F. Herbst, R. W. Lee, F. E. Pinkerton, Pr-Fe and Nd-Fe-based materials: A new class of high-performance permanent magnets (invited). *Journal of Applied Physics*. **55**, 2078–2082 (1984).
17. I. C. on N.-I. R. Protection, GUIDELINES FOR LIMITING EXPOSURE TO TIME-VARYING ELECTRIC AND MAGNETIC FIELDS (1 Hz TO 100 kHz). *Health Physics*. **99**, 818–836 (2010).
18. Guidelines for Limiting Exposure to Electromagnetic Fields (100 kHz to 300 GHz). *Health Physics*. **118**, 483–524 (2020).
19. O. Cugat, J. Delamare, G. Reyne, Magnetic micro-actuators and systems (MAGMAS). IEEE Transactions on Magnetics. 39, 3607–3612 (2003).
20. D. Niarchos, Magnetic MEMS: key issues and some applications. Sensors and Actuators A: Physical. 106, 255–262 (2003).

21. B. Paden, B. Norling, J. Verkaik, Telemetry method and apparatus using magnetically-driven mems resonant structure (2007), United States Patent US20070236213A1.
22. A. Aburub, M. Fischer, M. Camilleri, J. R. Semler, H. M. Fadda, Comparison of pH and motility of the small intestine of healthy subjects and patients with symptomatic constipation using the wireless motility capsule. *International Journal of Pharmaceutics*. **544**, 158–164 (2018).
23. W. Andrä *et al.*, A novel magnetic method for examination of bowel motility: Magnetic tracking of bowel motility. *Med. Phys.* **32**, 2942–2944 (2005).
24. E. Stathopoulos, V. Schlageter, B. Meyrat, Y. de Ribaupierre, P. Kucera, Magnetic pill tracking: a novel non-invasive tool for investigation of human digestive motility. *Neurogastroenterol. Motil.* **17**, 148–154 (2005).
25. A. M. Edwards, N. A. Clark, Thermoregulatory observations in soccer match play: professional and recreational level applications using an intestinal pill system to measure core temperature. *Br J Sports Med*. **40**, 133–138 (2006).
26. C. McGugin *et al.*, Radiofrequency identification tag localization is comparable to wire localization for non-palpable breast lesions. *Breast Cancer Res Treat*. **177**, 735–739 (2019).
27. L. R. Lamb, M. Bahl, M. C. Specht, H. A. D'Alessandro, C. D. Lehman, Evaluation of a Nonradioactive Magnetic Marker Wireless Localization Program. *American Journal of Roentgenology*. **211**, 940–945 (2018).
28. P. G. Seiler, H. Blattmann, S. Kirsch, R. K. Muench, C. Schilling, A novel tracking technique for the continuous precise measurement of tumour positions in conformal radiotherapy. *Phys. Med. Biol.* **45**, N103–N110 (2000).
29. M. Liebl *et al.*, Noninvasive monitoring of blood flow using a single magnetic microsphere. *Sci Rep*. **9**, 1–8 (2019).
30. B. Gleich, I. Schmale, T. Nielsen, J. Rahmer, Data and Code for Needle Tracking and Temperature Sensing with Miniature Magneto-Mechanical Resonators, Version 1, Zenodo (2023); https://doi.org/10.5281/zenodo.7664908.
31. B. F. Edwards, D. M. Riffe, J.-Y. Ji, W. A. Booth, Interactions between uniformly magnetized spheres. *American Journal of Physics*. **85**, 130–134 (2017).
32. H. Kaden, *Wirbelströme und Schirmung in der Nachrichtentechnik* (Springer-Verlag, Berlin Heidelberg, ed. 2, 2006, *Klassiker der Technik*.
33. CardioMEMS^{TM} HF System Model CM1000 Patient System Guide (2014).
34. M. Allen, M. Fonseca, J. White, J. Kroh, D. Stern, High Q factor sensor (2006), United States Patent USOO7147604B1.

Acknowledgments:

The authors thank the Müller family for providing and handling the bees, our students for their contributions, our colleagues for hardware support, medical devices, and CT measurements, the reviewers for their feedback, and the internal project sponsors for their continued backing.

Funding: none declared

Author contributions:

Conceptualization: BG, JR

Methodology: BG, JR, TN

Investigation: JR, BG, IS, TN

Evaluation: JR, TN

Visualization: JR, BG

Project administration: JR

Writing – original draft: JR, BG

Writing – review & editing: BG, IS, TN, JR

Competing interests: All authors are employees of Philips GmbH Innovative Technologies Research Laboratories Hamburg. Philips has submitted the following patent applications regarding the presented technology: US20220257138, US20220238011, US20220175487, US20210244305, US20200397320, US20200397530, US20200397510, US20200400509.

Data and materials availability: All data necessary to understand and assess the conclusions are available in the manuscript and the supplementary material. Additional data and evaluation code are accessible online (*30*).

Supplementary Materials

Materials and Methods

Supplementary Text

References (*31–34*)

Figs. S1 to S8

Movies S1 to S10

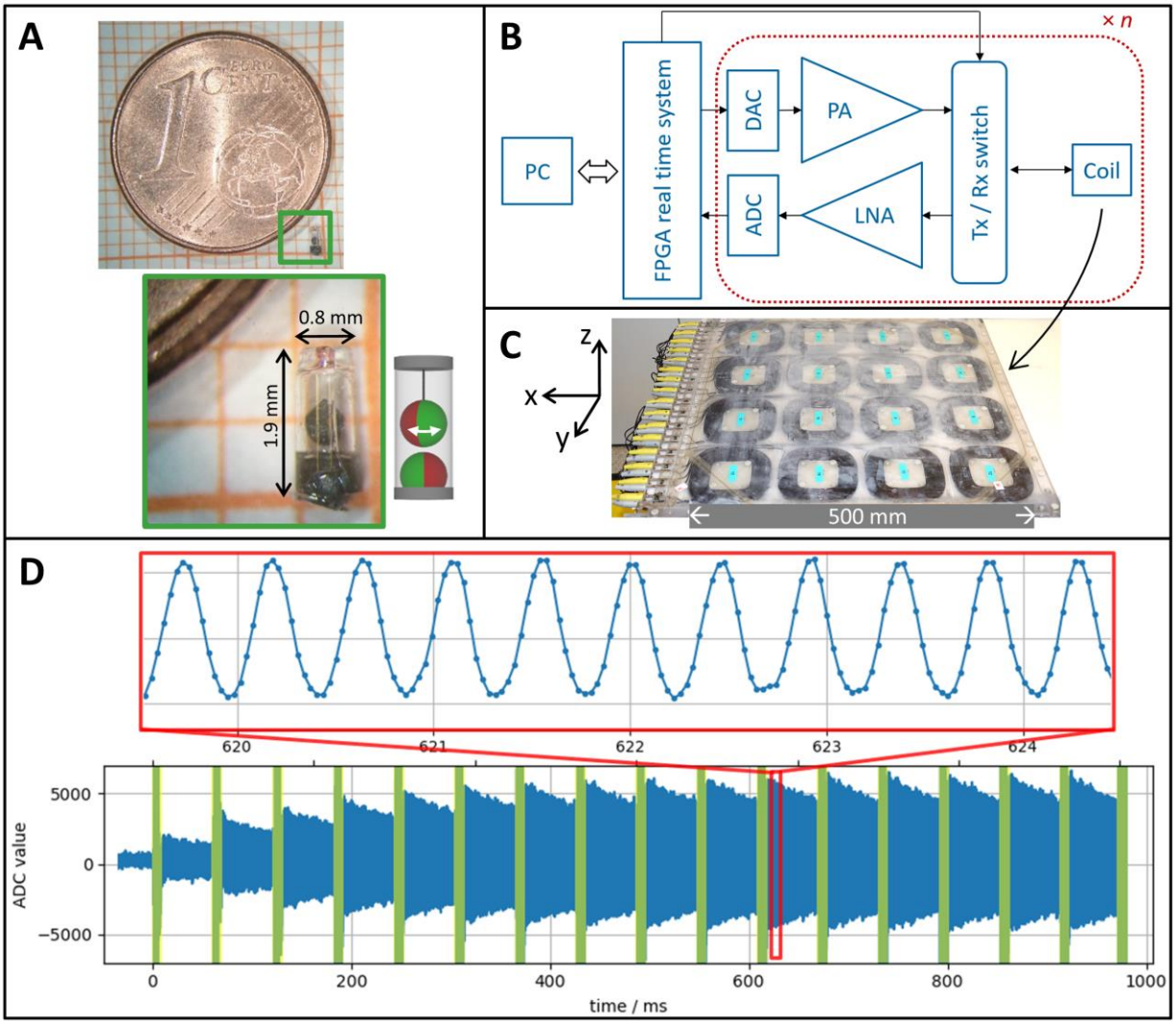

Fig. 1: MMR system components and signal response. (**A**) MMR demonstrator in relation to a coin (1 Euro Cent, diameter 16.25 mm) and sketch of its design. The suspended magnetic sphere (diameter 0.5 mm) can perform a rotational oscillation (white double arrow, cf. Movie S1) about the long axis of the cylinder, which has a volume of 0.96 mm³. In equilibrium, the spheres have anti-parallel alignment (red – magnetic north pole, green – south pole). (**B**) Schematic of transmit / receive (Tx / Rx) detection system with *n* channels. A field-programmable gate array (FPGA) is used for real-time control of the Tx and Rx data streams. The transmit pulse trains are generated by digital-to-analog converters (DAC) and sent via power amplifiers (PA) to the coils of the array. The receive signals pass through low-noise amplifiers (LNA) to the analog-digital converters (ADC) connected to the FPGA. A switch protects the receive path during application of the excitation pulses. (**C**) 4×4 coil array used for MMR excitation and detection of its spatial signal profile. (**D**) Overview and magnification of a typical MMR time signal. Brief excitation windows (overlaid by yellow-green boxes) alternate with receive periods during which signal decays. Starting from equilibrium, excitation pulses are played repeatedly with correct timing to build up the oscillation amplitude over several transmit / receive cycles.

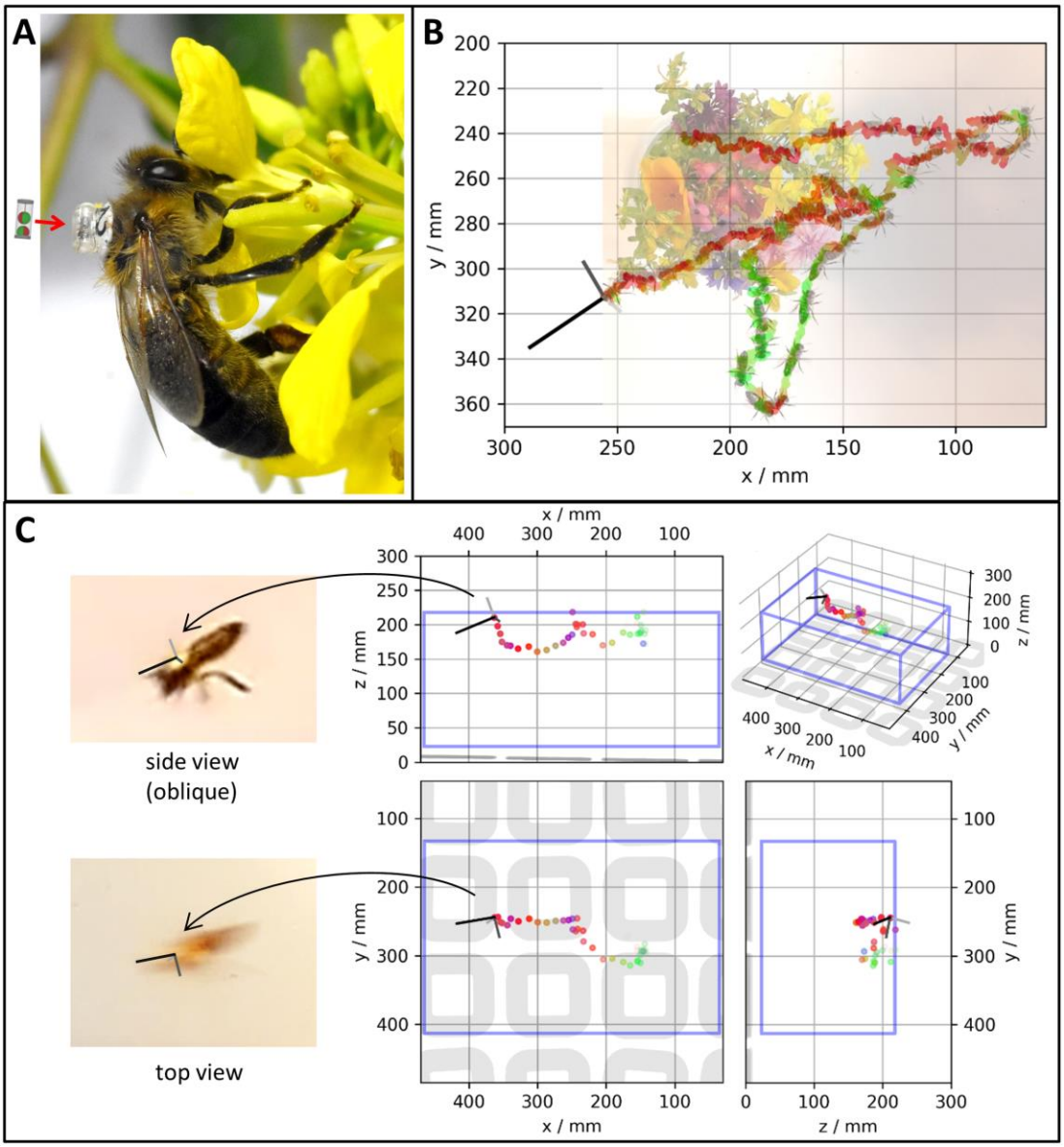

Fig. 2: Bee tracking experiments. (**A**) A honeybee equipped with an MMR marker. (**B**) Tracked path of a bee walking upside down below the transparent lid of a box garnished with a bunch of meadow flowers. The lid is about 20 cm above the planar 4x4 coil array used for detection. The path of the bee reconstructed from the MMR signal is plotted with an overlay of images extracted from a video sequence (see Movie S2). The black and gray lines indicate the bee's attitude in space for the last displayed measurement, while the previous orientations of the long bee axis (black line) are color coded in the plotted path (red / green / blue line color = bee axis aligned along *x* / *y* / *z* direction). (**C**) Brief segment of a tracking experiment of a flying bee. Right: The graphs show orthogonal projections of the reconstructed bee positions to visualize the 3D flight path relative to the box (indicated by violet lines). From each measurement, position and attitude of the bee is obtained as shown by the lines plotted at the last position (black = long axis of bee, dark gray = lateral axis, light gray = vertical axis). Left: Extracted movie frames show the good correlation of the attitude obtained from MMR tracking with the attitude seen by the two cameras.

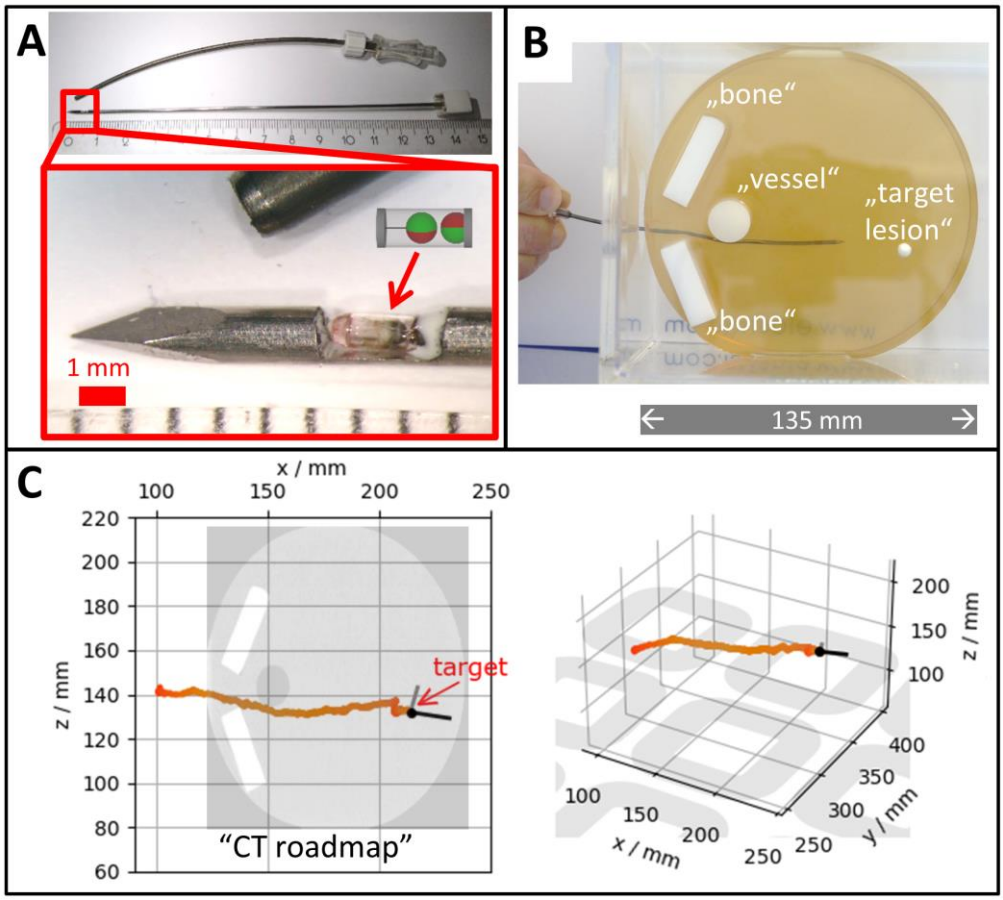

Fig. 3: Curved needle navigation experiment. (**A**) For demonstration, the MMR is glued into a recess cut into a flexible stylet that is inserted into a curved biopsy needle. The diameter of the MMR housing is 0.8 mm, the diameter of the stylet is 1.3 mm, and the outer diameter of the needle is 1.65 mm (16G Birmingham gauge). (**B**) Gelatin phantom simulating a patient. Two “bones” and one “vessel” block direct access to the “target lesion”. (**C**) Projection and oblique view of reconstructed needle path inside the phantom (cf. Movie S4). The black dot marks the needle tip derived from the MMR position and orientation. The black line points along the needle axis, and the gray line marks the axial rotation to enable controlled needle rotation. For navigation, a slice of a 3D CT data set of the phantom has been projected (and is therefore deformed) on the *xz* view. The shaky course of the needle is mainly caused by stick-slip movement of the needle in the rather hard Gelatin phantom material.

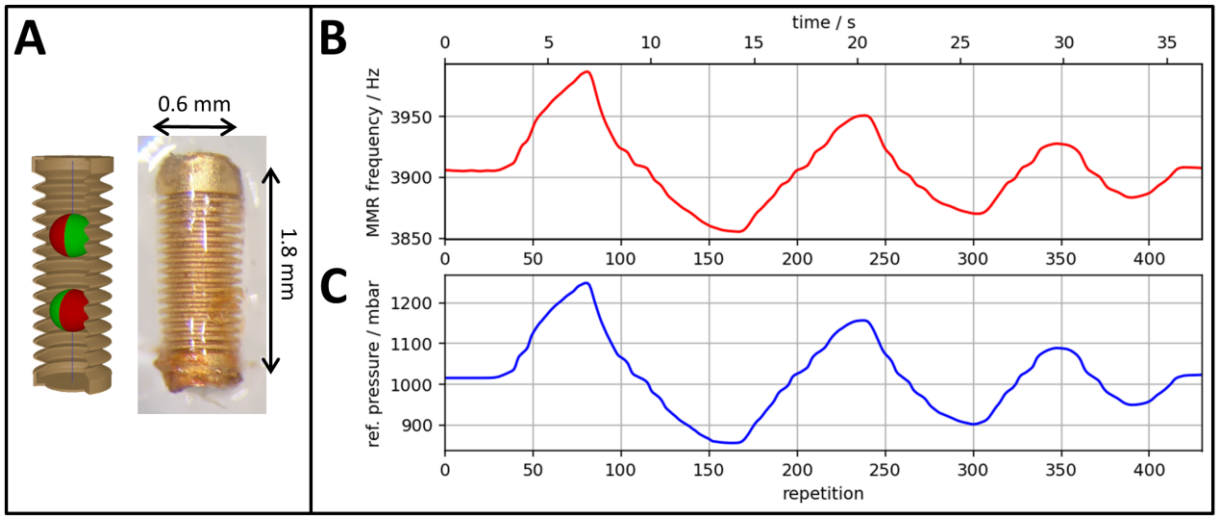

Fig. 4: Pressure sensor design, demonstrator, and measured pressure variation. (**A**) A compressible housing translates outer pressure variations to distance changes between two oscillating spheres. The diffusion-tight metal housing of the demonstrator provides the required stiffness and is coated with silicone rubber for a biocompatible surface. The sensor volume is 0.51 mm³. (**B**) Application of external pressure using a manually operated syringe changes the resonance frequency of the MMR. Thereby, an increasing pressure reduces the MMR inter-sphere distance and increases the frequency. The MMR is placed at about 70 mm above the coil array. (**C**) For reference, a commercial pressure sensor provides the applied pressure.

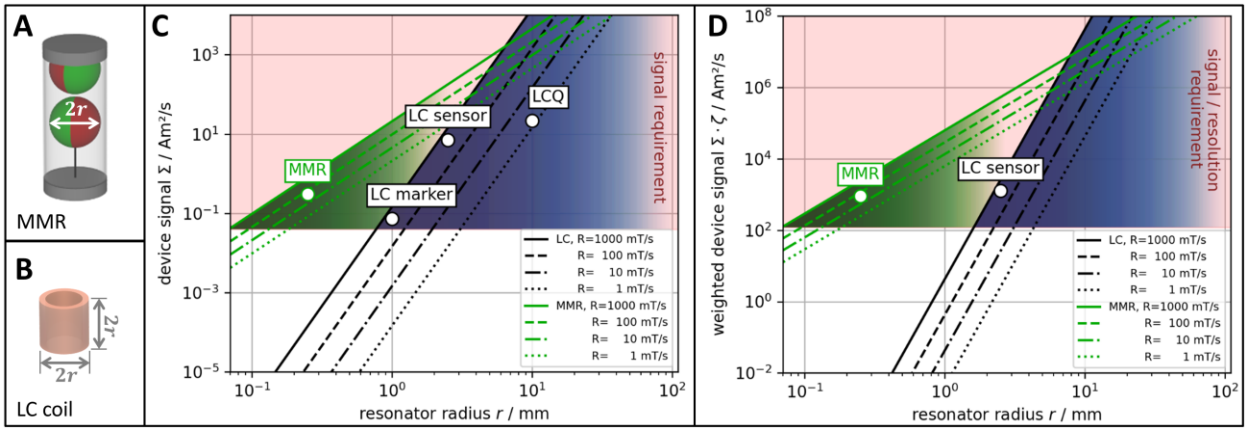

Fig. 5: Signal scaling comparison between MMR and LC-type resonators for marker and sensor applications. For markers, device signal Σ determines tracking performance, whereas for sensors, performance depends on signal Σ multiplied with a quality function ζ that reflects frequency resolution. (**A**) The "resonator radius" r corresponds to the radius of the oscillating MMR sphere. (**B**) For LC resonators, r is the radius of a cylindrical antenna coil of height $2r$ and conductor thickness r/4. (**C**) Double logarithmic plot of signal Σ from MMRs (green lines) and LC resonators (black lines) for different applied rates of field change R (different dash styles). A minimal signal requirement for detecting the devices up to reasonable distances of about 20 cm in an unshielded environment is shaded in light red. The blue area indicates where LC resonators can be operated. The green area shows the region only accessible to the MMR technology. The circles annotated with "MMR" and "LCQ" illustrate values of the marker demonstrators (supplementary materials) presented in this work, while "LC marker" and "LC sensor" represent typical values of optimized devices. (**D**) Double logarithmic plot of weighted device signal $\Sigma \cdot \zeta$. While for MMRs, the quality function ζ is a constant factor, for LC sensors, it scales with the squared coil radius. The resulting limited frequency resolution prevents shrinking LC sensor size below a few millimeters.